Large-scale volumetric characterization of a turbulent boundary layer flow

Conference Paper · July 2019

6 authors, including:

Daniel Schanz
German Aerospace Center (DLR)
249 PUBLICATIONS   2,209 CITATIONS

SEE PROFILE

Andreas Schröder
German Aerospace Center (DLR)
579 PUBLICATIONS   3,856 CITATIONS

SEE PROFILE

Matteo Novara
German Aerospace Center (DLR)
90 PUBLICATIONS   1,118 CITATIONS

SEE PROFILE

Janos Agocs
German Aerospace Center (DLR)
141 PUBLICATIONS   449 CITATIONS

SEE PROFILE

Large-scale volumetric characterization of a turbulent boundary layer flow

Daniel Schanz[1]*, Matteo Novara[1], Reinhard Geisler[1], Janos Agocs[1], Felix Eich[2], Matthew Bross[2], Christian J. Kähler[2], Andreas Schröder[1]

[1]German Aerospace Center (DLR), Inst. of Aerodynamics and Flow Technology, Göttingen, Germany

[2]Universität der Bundeswehr, Inst. of Fluid Mechanics and Aerodynamics, München, Germany

*daniel.schanz@dlr.de

Abstract

We report on an experimental undertaking with the goal of detecting so-called turbulent superstructures within a turbulent boundary layer and describing their temporal development while propagating from a region of zero pressure gradient (ZPG) into a region of adverse pressure gradient (APG). The flow was characterized by performing Lagrangian Particle Tracking (LPT) of Helium-filled soap bubbles (HFSBs) using the Shake-The-Box (STB, Schanz et al. 2016) algorithm.

This work will present first results, but will concentrate on the description of the experimental efforts and the evaluation approaches that were necessary to successfully conduct this investigation. The tracking of a large number of tracer particles (several 100,000) within an extensive volume (nearly three meters in length) was made possible by the use of a system consisting of 12 cameras, forming three successive volumetric systems. Calibration and evaluation methods for fusing the different systems into one large camera system are described. Challenges in calibrating camera systems with a large field-of-view due to small-scale distortion effects introduced by the observation windows are discussed and correction methods are introduced. Methods for achieving a perfect transition between overlapping camera systems are introduced.

For higher flow velocities, a double illumination approach was created in order to limit the pixel displacement between frames. To the knowledge of the authors, this is the first time such an approach was realized for time-resolved image sequences.

1   Introduction

The understanding of the formation and the dynamics of very-large scale coherent structures within turbulent boundary layers (TBLs) and their influence on the wall shear stress and intermittency is an important research topic in aerodynamic flows at high Reynolds numbers not attainable by DNS. Amongst others, Jimenez (1998) showed that eddies with streamwise lengths of 10-20 δ are present in the upper logarithmic region of wall-bounded flows. In addition to TBLs and turbulent channel flows, Kim and Adrian (1999) found streamwise energetic modes with wavelengths up to 14 pipe radii within fully developed turbulent pipe flow. The characterization of these large-scale coherent motions, often referred to as superstructures in TBLs and very large scale motions (VLSMs) in turbulent pipe or channel flow, has since been the subject of numerous experimental investigations, which successfully detected and described partial views and features of these large scale coherent structures (e.g. Hutchins and Marusic 2007 and Marusic et al. 2010). However a full spatiotemporal experimental investigation was still pending. Such an experimental undertaking will be presented in the following, here concentrating on the applied and developed measurement techniques.

2   Experimental setup

The experiment was set up in the 22m long test section of the Atmospheric Wind Tunnel (AWM) at the University of the Armed Forces in Munich (see Figure 1 a). A model was installed at the side wall of the 1.8×1.8 m² cross section (Figure 1 b and c). The flow develops on the wind tunnel wall over a few meters and is then
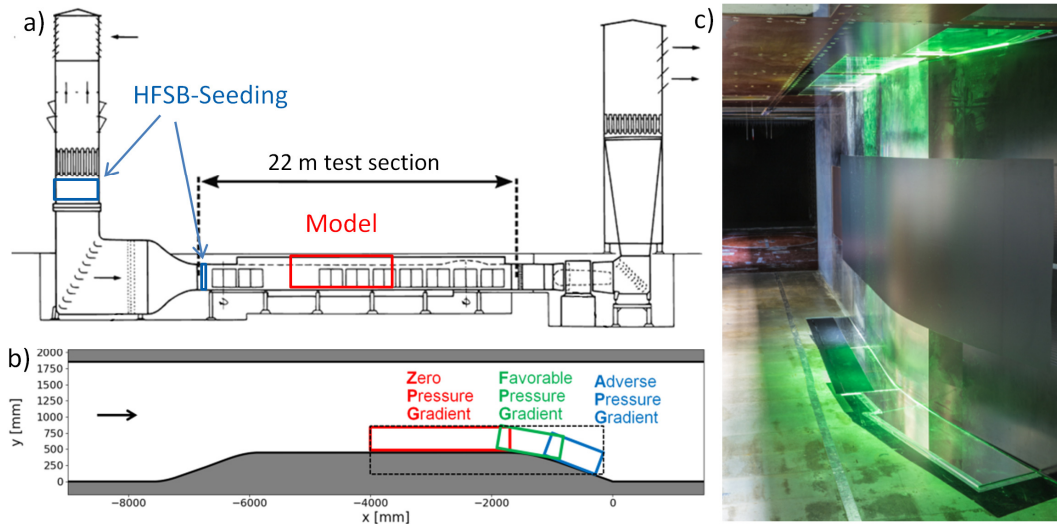

Figure 1: a) Cutaway of the Atmospheric Wind tunnel at the Univerität der Bundeswehr in Munich (AWM). The approximate location of the model (installed up-right on the wind tunnel wall) is given by the red rectangle; b) Sketch of top view of the model with the different pressure gradient regimes; c) Photograph of the installed model from a downstream position, showing the deflection leading into the APG region. LED Illumination from above, back-reflected by mirrors on the floor.

accelerated in a FPG region along a ramp of 1.20 m length with smooth curvatures. Next, the flow develops gradually into a canonical ZPG boundary layer state along a flat plate of length 4.0 m. The TBL flow then follows two curvilinear deflections over a length of 1.17 m, causing a small FPG, and enters into the APG region of a subsequent flat plate with an inclination angle of 18° and length of 763 mm.

A system of twelve high-speed cameras was installed outside of the tunnel, opposite to the model. Three overlapping volumetric subsystems (see Figure 2) covered a continuous volume from the middle of the ZPG plate to the APG region (~2.90 m stream-wise, 0.8 m span-wise and 0.25 m wall-normal). The cameras were operated at a constant repetition rate of 1 kHz and recorded continuous data for 1382 images. The most upstream camera system (A) consisted of four VEO 4K L cameras, which provide a 4096×2160 pixel resolution at 1 kHz. Due to the high spatial resolution and the elongated shape of the sensors, this system was able to capture the full ZPG-region at a length of 1.80 m, using f=35 mm Carl Zeiss Distagon lenses, mounted in Scheimpflug-adapters. The two subsequent systems (B and C) each consisted of four PCO DiMax cameras (2016×2016 pixel) and each covered around 1 m in stream-wise direction, being equipped with f=50 mm Carl Zeiss Planar lenses. The magnification is between 2.0 to 2.5 px/mm for the whole system.

The wall-normal extent of the recorded volume is defined by the illumination, consisting of 10 high-power LED arrays (Hardsoft ILM 501CG, Stasicki et al. 2017), installed above window inserts on the wind tunnel roof. Mirrors at the wind tunnel floor provided back-reflection (Figure 1 c).

Three different free stream velocities U_{fs} were considered: $U_{fs} \approx 7$, 14 and 21 m/s. At the lowest velocity, particle shifts of around 19 pixels are found in the free stream. In order to limit the shift for higher velocities, a double illumination scheme was applied, motivated by its successful application on double frame cameras for the investigation of high-speed flows (Novara et al. 2019). While the

cameras retained the rate of 1 kHz, the LEDs were operated at 2 kHz, thus imaging each particle twice per camera image.

Seeding of the flow was realized by several arrays of HFSB-nozzles (250 nozzles in total). For the lower velocity, most of the seeding rakes (200 nozzles) were installed close to the contraction before the test section. While ensuring a high seeding concentration, a downside of this position is an interaction of the rakes with the incoming boundary layer that might persist in the measurement
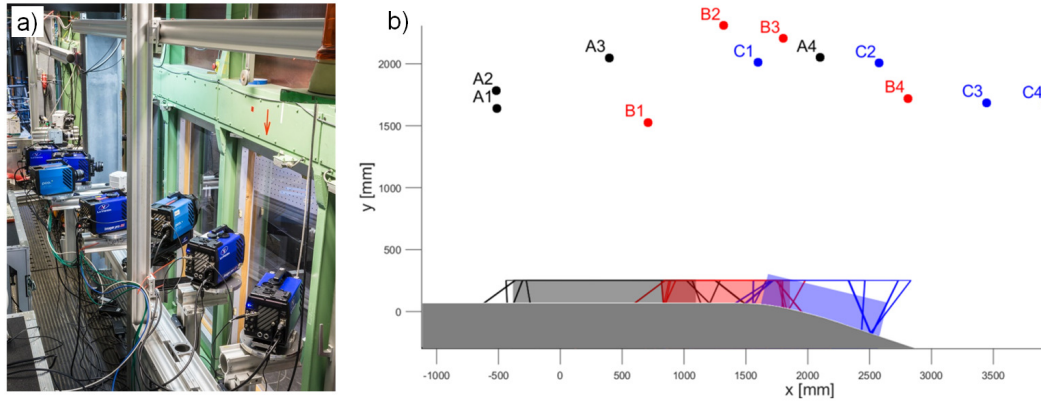

Figure 2: a) View of the twelve-camera system outside the AWM tunnel; b) Schematic sketch of the camera positions, viewed from the top. Three camera systems are indicated in black (A), red (B) and blue (C). Flow from left to right, the model geometry is indicated in dark grey

region. Therefore, for the more relevant runs at higher Reynolds numbers, the seeding system was moved much further upstream, into the tower of the wind tunnel. Now the bubbles had to pass through several layers of meshes, minimizing any flow disturbances, but also reducing the number of bubbles reaching the measurement volume. In both cases, 50 additional nozzles were installed in a cabinet close to the contraction region, seeding the near-wall parts of the boundary layer through a thin slit in the wind tunnel wall.

For the $U_{fs} \approx 7$ m/s case 24 runs of 1382 images each were recorded in single illumination mode. The particle image density visible on the camera images varies locally, depending on the amount of tracer particles and the local strength of illumination. Typically values between 0.04 and 0.06 particles per pixel (ppp) are detectable. Figure 3, Left shows a typical particle image distribution. The attained image quality (signal to noise ratio) is high, with peak intensities typically ranging from 500 to several thousand counts. The illumination is well sufficient, even though the LEDs were operated only in short bursts of 40 µs per image (4 % duty cycle, at 45 A power), in order to avoid any motion blurring for the fastest particles.

At the two higher velocities, the seeding concentration is reduced, both due to the increased mass flow and the repositioning of the main seeding system. However, the recorded particle image density is doubled due to the two light pulses. Figure 3, Middle shows a sub-sample of a typical camera image of such a case, while Figure 3, Right shows a region with low seeding density in order to better visualize that each particle is imaged twice per camera image. For $U_{fs} \approx 14$ m/s, being the central case for the physical evaluation, 68 runs of 1382 recordings (corresponding to 2764 time-steps) were recorded.
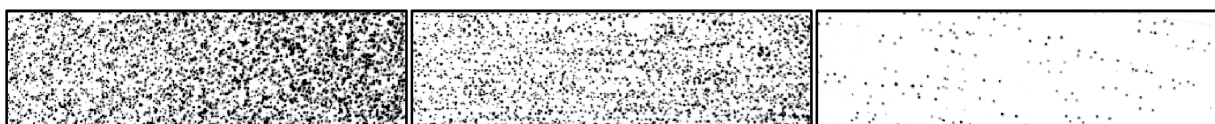

Figure 3: Excerpts from camera images. Left: Single-illuminated run at $U_{fs} \approx 7$ m/s. Middle: double-illuminated run at $U_{fs} \approx 14$ m/s., center of the volume. Right: same, corner of the volume with less particles and illumination, showcasing double images per particle. In all cases, preprocessing consisted of subtracting the minimum image and a constant.

3 Data evaluation

Particle tracking was performed using the current DLR implementation of the Shake-The-Box (STB) algorithm. For the required 3D calibration a large 2D target, oriented parallel to the flat plate, was imaged by all cameras simultaneously at two wall-normal planes, separated by 100 mm. This rough calibration was refined using Volume Self Calibration (Wieneke 2008), calibration of the optical transfer function (OTF, Schanz et al. 2013) and several specifically adapted procedures to ensure optimal overlap of the up to 8 calibrated camera models in the common regions and to correct for distortion effects of the wide-angle lenses and the wind tunnel windows. Chapter 5 gives a detailed overview of the special calibration procedures developed for this evaluation.

3.1 Triangulation approach for extensive multi-camera systems

The thorough calibration allowed to treat the whole camera-system as one within the STB-procedure: The specific implementation of the triangulation procedure, being a central part of the iterative particle reconstruction (IPR) within each STB-step, can be operated with an arbitrary number of cameras N_{cam} and returns the triangulated 3D positions of all particles visible in at least N_v cameras, where N_v is specified by the user. In this case, all cameras from the three subsystems were included in the triangulation process ($N_{cam} = 12$) and particles were retrieved that either fulfill $N_v \geq 4$ (first two iterations of IPR) or $N_v \geq 3$ (last two iterations of IPR). The result is a cloud of triangulated particles that are seen by at least three cameras, spanning over the whole volume.

3.2 Particle tracking in single-illuminated cases

When applying the Shake-The-Box algorithm to the preprocessed camera images, the combination of high image quality and a very refined calibration allows using a restrictive parameter of 0.7 px for the search radius in the triangulation process, thereby limiting the creation of ghost particles as much as possible. Still, for the first images, a total amount of particles (real and ghosts) of $\sim$ 1.55 million is reconstructed. From these particle clouds $\sim$251,000 4-time-step tracks are extracted. Figure 4 left) illustrates the convergence of the tracking system. The found tracks help in reducing the perceived seeding density and act as a predictor for the search for new tracks. This way, the system quickly identifies more and more trajectories. Within 10 time-steps $\sim$443,000 particles are tracked, after 70 time-steps the system reaches a maximum of $\sim$580,000 tracked particles. From there on the system is stable, the visible decline in tracked particles is caused by variations of the particle density. At the end of this 300-recording test-run, the algorithm reverses the time-series and walks backwards for a second pass. Triangulation is not performed anymore, only the known tracks from pass 1 are elongated into regions where they have not been tracked yet in the first pass. This approach increases the number of tracked particles per time-step by approx. 33.000. The convergence region is effectively filled up and a maximum number of $\sim$620,000 tracked particles per time-step is achieved.
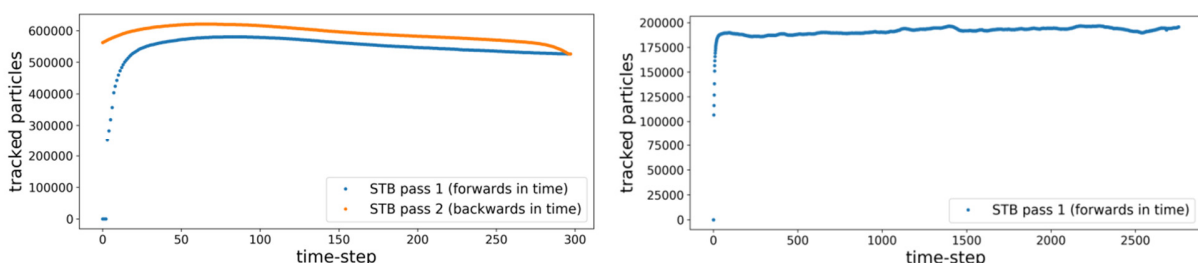

Figure 4: (left) Number of tracked particles per time-step for STB evaluation over a time-series of 300 images (single illumination mode at 7 m/s), first going forward in time (pass 1), then reversing and elongating found tracks in backwards direction (pass 2). Up to 620,000 particles are tracked.

(right) Number of tracked particles per time-step for an STB evaluation in double illumination mode at 14 m/s. 1382 images yield 2764 time-steps. Up to 200,000 particles are tracked per time-step.

3.3 Particle tracking in double-illuminated cases

For the double illumination images, the STB scheme had to be modified: Firstly, the trajectories known in time-step N are extrapolated to both time-steps t_{N+1} and t_{N+2} imaged in the next snapshot and the resulting particle cloud is corrected for inaccuracies by shaking. Now IPR is applied to identify new particles. Next, fitting particles to extend the know tracks to the *first* time-step t_1 are searched within all (twice predicted and triangulated) particles. Now the tracks known in t_{N+1} are again predicted to t_{N+2}, where they form a particle cloud together with the already precisely know tracked particles from t_{N+1} (which are also imaged and therefore have to remain in the volume). This cloud is again treated by shaking and IPR triangulations. As a last step, fitting particles to extend the know tracks to the *second* time-step t_2 are searched within the particle cloud. By applying this scheme of double extrapolation and shaking, an unfavorable treatment of the second time-step is avoided. If the known tracks were simply elongated to t_{N+1} and t_{N+2}, followed by a normal STB treatment, the extrapolation of t_{N+2} would cover such a large separation (up to 60 pixels) that the errors would not always be recoverable by the shaking process, resulting in an enhanced loss of tracks within each second time-step. The described scheme avoids this effect and was implemented in a way that an arbitrary number of illuminations per image can be processed.

Figure 4 right displays the convergence of STB for a double-illuminated time-series of 1382 images, corresponding to 2764 time-steps at 2kHz recording rate. The tracking system starts with ~110,000 4-step tracks and quickly converges to 190,000 to 200,000 tracked particles, corresponding to 380,000 to 400,000 imaged particles within each recording of the combined camera system .

3.4 Data postprocessing

The raw particle positions are filtered by a spline-interpolation scheme ('TrackFit', Gesemann at al. 2016), yielding continuous position, velocity and acceleration. The gained data can be used in many ways: volumetric averages can be created using a bin-averaging approach; one-point statistics (e.g. PDFs), space-time spectrum, two-point correlations or Lagrangian properties can be extracted. As the tracks represent a spatially dense sampling of the flow, the instantaneous flow field can be reconstructed using the 'FlowFit' algorithm (Gesemann et al. 2016). This method allows to further increase the spatial resolution by incorporating physical constraints into the reconstruction process on a volumetric grid of cubic B-splines.

4   Results

Figure 5 shows exemplary results from an evaluation at $U_{fs} \approx 7$ m/s. The full field (top) visualizes the dense tracking of approx. 620,000 particles. It can be seen that the flow reaches approx. 7 m/s above the flate plat, is slightly accelerated in the suction peak of the FPG and clearly decelerates in the APG region.

By applying the FlowFit algorithm to the discrete particle cloud, flow structures can be identified (middle). Despite the large measurement domain, medium-scale structures in the outer parts of the boundary layer are well resolved, as a result of the dense particle tracking and the further increase in spatial resolution by the data assimilation approach. Close to the wall, where structures become smaller and smaller, undersampling of the flow gradients is evident, as expected given the large observation space and the bubble diameter of 300 μm. The results gained by FlowFit can be used, among others, for analyzing the interaction of superstructures with smaller scales.

When displaying a wall-parallel slice of the particle field, approximately centered around 0.4 boundary layer thicknesses (bottom), elongated structures of low and high relative velocity can be seen, reaching from the ZPG into the FPG and APG domains. The identification and analysis of the spatio-temporal development of these structures will be the main topic of the upcoming investigations.

The gained velocity- and acceleration information at the discrete locations of the particles can be used to generate statistical results by defining bins and averaging the properties of all particles found within a certain bin over a time-series. Figure 6 shows a first result of this approach (using only 200 images), where the bins were extending over the whole spanwise domain. The resolution in streamwise and wall-normal direction was 4×4 mm^2.
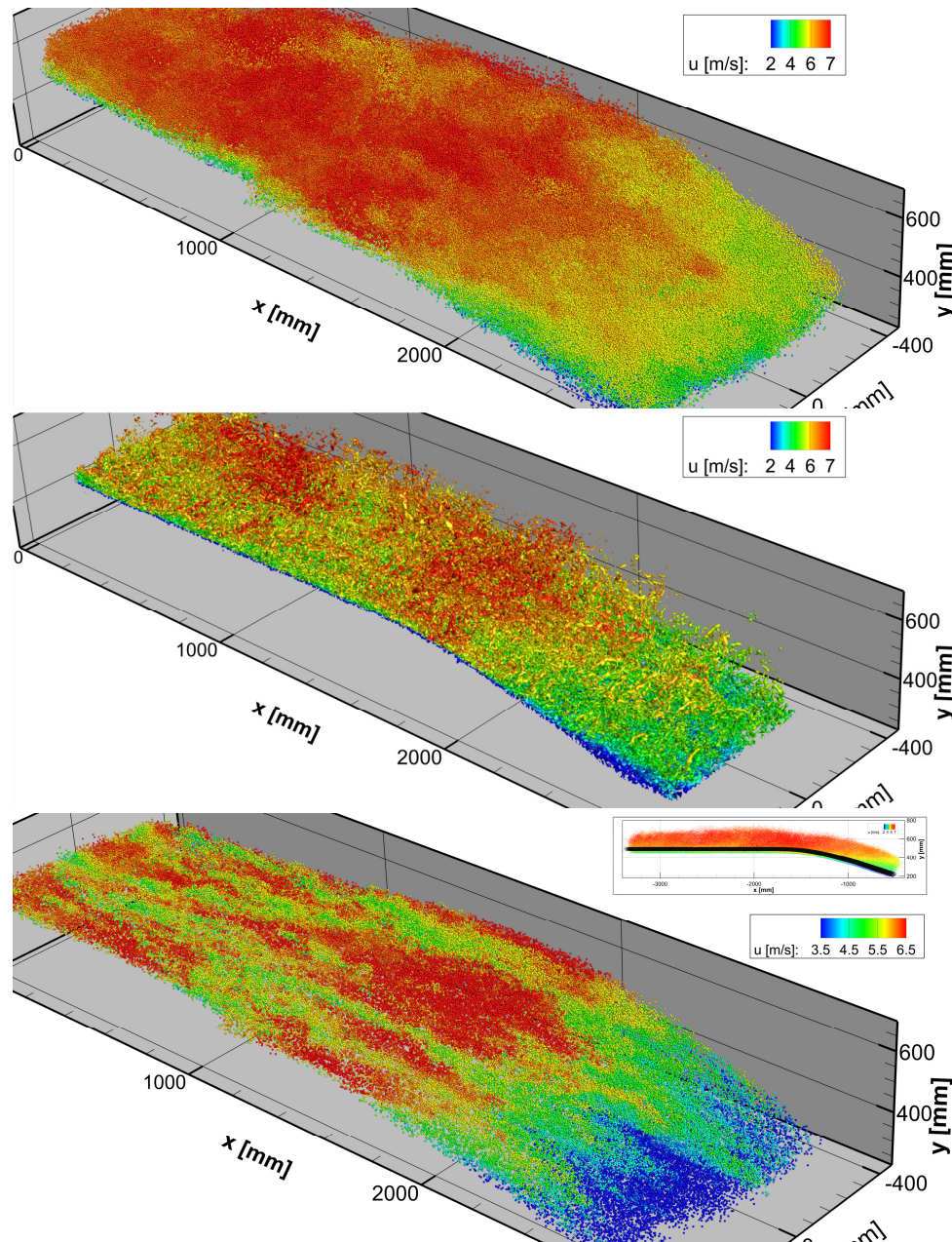

Figure 5: Exemplary instantaneous evaluation result at U_{fs} = 7 m/s. (top) 620,000 tracked particles, color-coded with streamwise velocity; (middle) FlowFit interpolation of the same particle cloud, visualized as isosurfaces of Q-criterion (Q = 2500/s); (bottom) wall-parallel cut (displayed region signified as the black area in the insert) through the particle field, showcasing large-scale structures.

The boundary layer of the ZPG-region can be recognized, though the near-wall region cannot be resolved. Resolving the near wall region requires seeding and recording concepts outlined e.g. in

Schröder et al. (2015) and Bross et al. (2019). When approaching the deflection region, the FPG causes an acceleration peak (see bottom figure) with a significant thinning of the boundary layer. Within the deflection the flow decelerates as the APG region is entered and the boundary layer thickens rapidly. Using the full dataset for such statistics will allow for much finer resolutions and/or the creation of 3D averages by using multiple bins in wall-normal direction, thus capturing e.g. three-dimensional side wall effects.
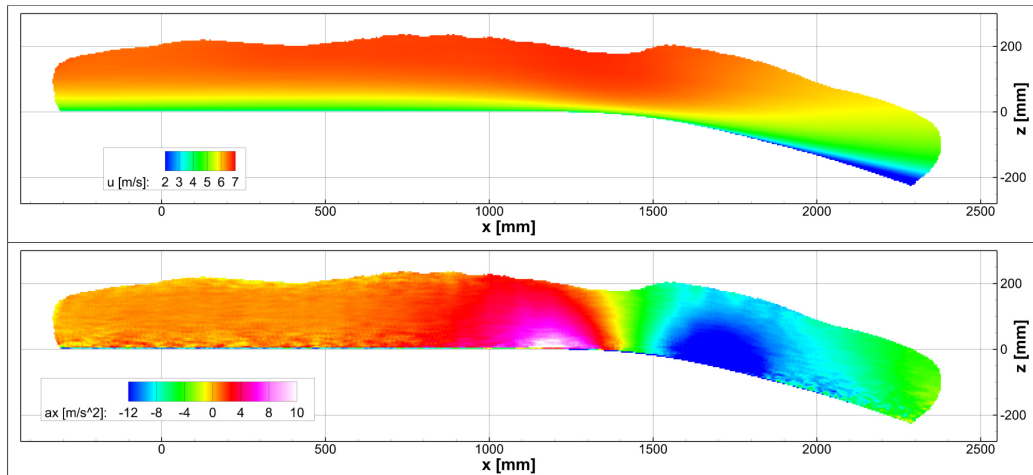

Figure 6: Average streamwise velocity (top) and acceleration (bottom) field based on 200 instantaneous samples.

Turning to the results of the double-illuminated cases at $U_{fs} \approx 14$ m/s (see Figure 7) it is evident that the double-illumination evaluation was equally able to seamlessly track the bubbles over the whole system. FlowFit interpolation shows a still detailed system of vortical structures; however the under-sampling is more evident in comparison to the slower case, as the particle number is reduced, while the spectrum of turbulent structures grows with increased Reynolds number. Animations still show a high degree of temporal coherence of the structures. Large-scale structures can again be easily identified by eye, when displaying the outer turbulent boundary layer region.
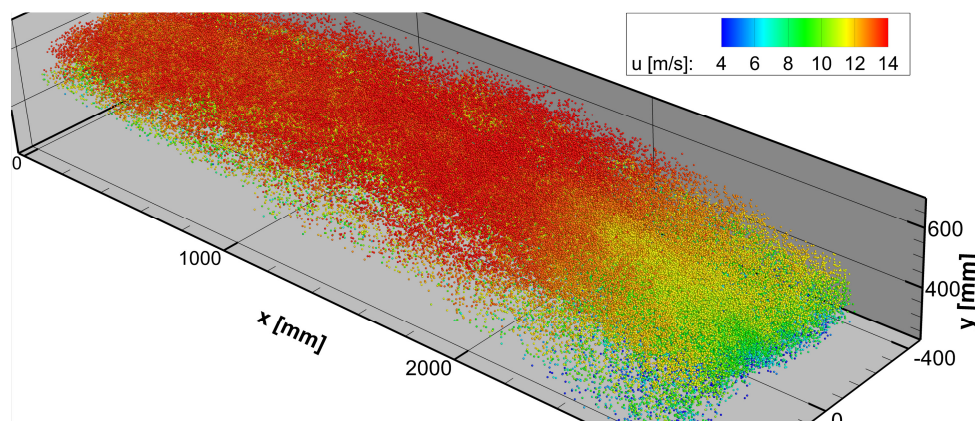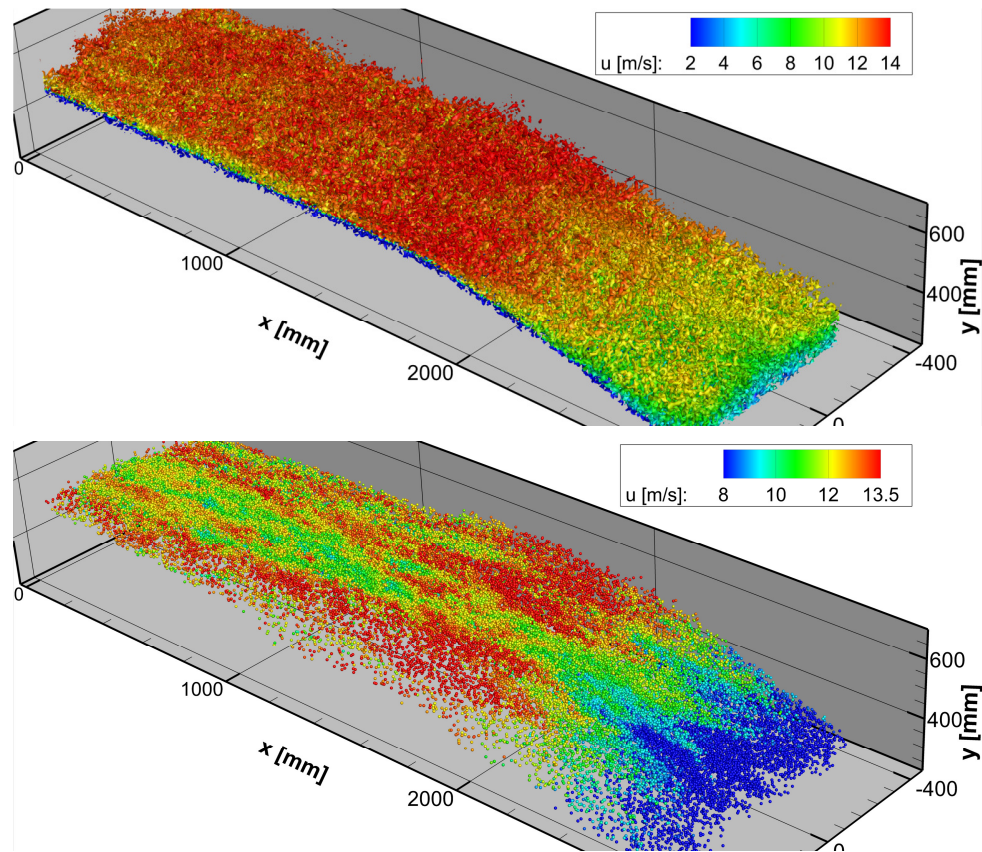
Figure 7: Exemplary snapshot of evaluation at U_{fs} = 14 m/s. (top) 200,000 tracked particles, color-coded with streamwise velocity; (middle) FlowFit interpolation of the same particle cloud, visualized as Isosurface of Q-criterion (Q = 2000/s); (bottom) wall-parallel cut of particle cloud.

5   Special calibration requirements

During the evaluation of the experimental data, certain issues with the viewing conditions of the cameras and the 3D calibration were discovered and correction methods were developed.

Volumetric experiments typically concentrate on flow measurements in relatively small volumes due to the available laser light. Only recently, with the growing use of Helium-filled soap bubbles as seeding material, much larger volumes became accessible. Such experimental setups, like the one described in the previous sections, typically make use of lenses with quite short focal lengths (24-50 mm). However, wide-angle lenses are much more prone to suffer from distortions (pin-cushion, barrel, moustache), compared to the more commonly used tele-lenses (60-180 mm) when imaging smaller volumes.

Commonly used calibration models approximate the viewing conditions from first order (e.g. the pin-hole model) to third order (e.g. polynomial models). However, even a third order model is often not able to capture all distortions introduced by wide-angle lenses up to the desired accuracy. In order to ensure reliable particle detection in the whole measurement volume, the calibration function of each camera has to be able to model the occurring imaging defects. Typically, the reprojection error should be kept below 0.1 pixels over the whole imaged volume.

Another factor that is often overlooked is that for many experiments the cameras are viewing the flow through glass or plexiglass windows. Depending on the quality of the glass (e.g. Schlieren), the lines-of sight can be slightly deflected, introducing fine-scale distortions. If the glass surface is curved (e.g. a pipe), the distortions can be massive (see e.g. Paolillo and Astarita, 2019).

Effects of the mentioned imaging problems were found within evaluated data from the large-scale boundary layer experiment. While the initial tracking results were promising, an interesting observation was made when looking at averaged results. Figure 8 shows a result of bin-averaging the properties of the tracked particles (comparable to Figure 6 bottom, albeit without any corrections). A pronounced stripy pattern is visible in the streamwise acceleration, which is clearly not of physical origin. Very distinct jumps in average acceleration can be observed at the transitions between different cameras (see the camera field-of views in Figure 8 bottom). This behaviour can be understood: The image distortions of wide-angle lenses are most severe at the border of the camera image. In case a particle transitions from being observed by a certain camera to not being observed anymore, this camera (and its potential remaining local decalibration) does not affect the particle position anymore. Therefore, the reconstructed trajectory exhibits a sudden jump, which is very visible in the average acceleration, even if its magnitude is low.
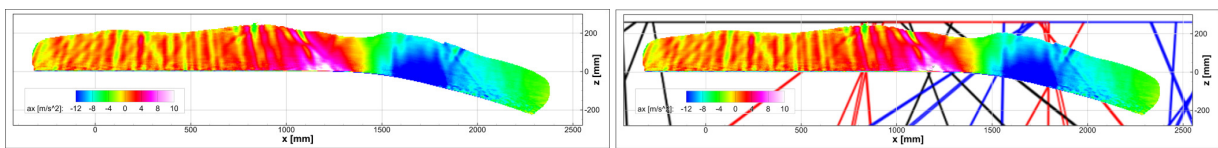

Figure 8: Averaged streamwise acceleration (left) and streamwise acceleration underlaid by camera field-of-views (right). Results gained by same bin averaging approach and time-series as in Figure 6.

However, the stripes in regions where no camera field-of-view is ending (especially visible in the region of the upstream flat plate) cannot be explained that way. The orientation of these stripes clearly follows the lines-of-sight of several cameras, most notably cameras A3 and A4 from the upstream system (see also Figure 2b).

This observation led to the conclusion that an effect on the camera images itself has to be the source of the artificial accelerations observed. In order to isolate each camera from any effects of the calibration or image processing, two-dimensional particle tracking was performed directly on the unprocessed images of all cameras, using measurement runs with low seeding concentration. The results were averaged in 10 × 10 pixel-bins.
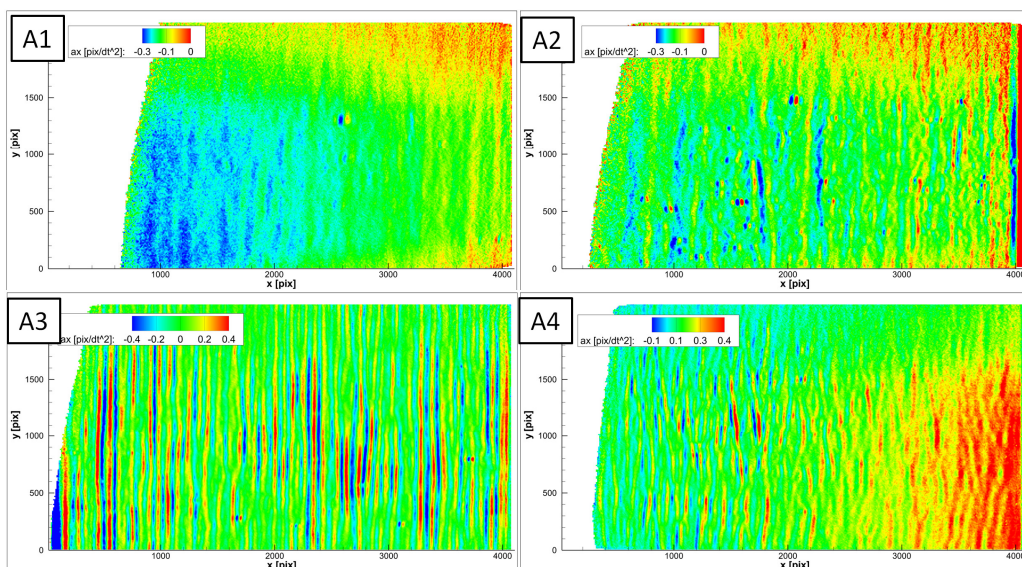

Figure 9: Results of 2D particle tracking on the unmodified source-images of cameras A1-A4. Average acceleration in units of pixels and time-steps (dt), calculated in bins of 10 × 10 px. Stripes of acceleration, originating from deviations of the optical paths, are evident, especially for cameras A3 and A4. The empty space to the left marks the end of the illuminated region.

Figure 9 shows the acceleration in x-direction (corresponding to the flow direction in world coordinates) of the 4 cameras of the A-system. Please note that due to the omission of any calibration, these results do not have any physical meaning. Due to the different angles of the cameras in relation to the measurement volume, the magnification varies over the field-of-view of each camera, leading to virtual accelerations. However, patterns of average acceleration are clearly defined, with camera A3 showing a very pronounced system of acceleration stripes and camera A4 showing a pattern of similar detail, albeit less organized. Cameras A1 and A2 are less effected, however they still show stripy patterns of lower frequencies.

The acceleration results in Figure 9 show a combination of physical effects, perspective projection and the discussed deflection pattern. In order to isolate the latter effect and to get a more quantitative description, a further processing is carried out.

Most of the particles located in a certain distance from the wall - above the log-layer - move at relatively straight paths, as they are only rarely subject to turbulent structures. In such a case, temporal smoothing with a long kernel can be used to dampen the high-frequency effects of the deflection fields, thus correcting the particle position, at least in a statistical sense. The qualified particle trajectories are identified by a velocity threshold on the 2D tracks and filtered using cubic B-splines ('TrackFit', Geseman et al. 2016) with a low cross-over frequency of 0.12. The found positions are subtracted from the originally found (image matched) positions, thus giving a measure in pixels of the deviation induced by fine-scale distortions, whose effects should be largely erased by the filtering.
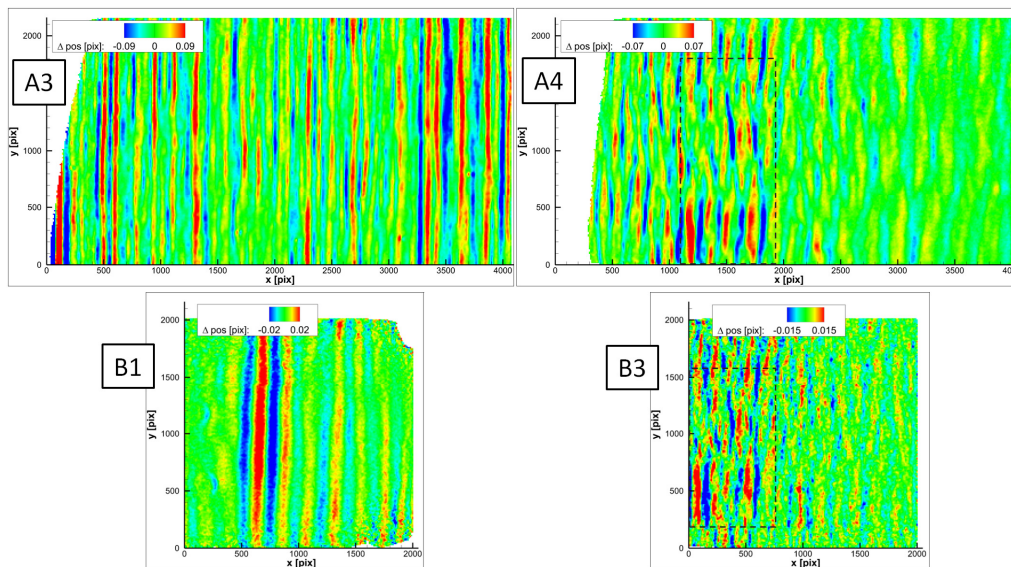

Figure 10: Results of 2D particle tracking on the unmodified source-images of cameras A3, A4, B1 and B3. Shown is the averaged deviation of the particle positions after a strong temporal filtering from the original positions (in x-direction). Fine-scale deviations can be isolated.

Figure 10 shows the bin-averaging results for this approach for cameras A3, A4, B1 and B4. The result for Camera A3 closely resembles the accelerations shown in Figure 9, as this camera is oriented nearly parallel to the window and flow. For camera A4 the virtual accelerations induced by the perspective imaging are gone and the small-scale deviations are isolated. Cameras A3 and B1 are viewing the flow through the same window, though they do not share a common field-of view. Still, the same vertical stripe pattern can be seen. B1 is located much closer to the window, which explains the stripes being much wider and lower in magnitude. Cameras A4 and B3 share a common field-of-view on another window. The marked box indicates a region, in which the found deviation

patterns clearly match between the two cameras, even if the magnitude is different (due to the different viewing conditions: distance and angle to the window, focal length, pixel size).

These findings clearly indicate that the glass windows of the wind tunnel are the origin of the observed acceleration patterns. Other sources of distortions can also be imagined, like the lens, the protective glass in front of the sensor or the positioning of the micro-lens array in relation to the silicon beneath. However, investigations if these play an additional role still have to be carried out. Localized spots of positive and negative acceleration are visible on all cameras, which are likely caused either by local defects in the window glass or by dust particles on the sensor cover glass.

5.2 Creating 2D correction maps

The deflections caused by the wind tunnel windows can be seen as an effect that is largely 2D, in that the deflection magnitude will be the same for all particles along a certain camera line-of-sight, regardless of the depth position.

Therefore, a 2D correction scheme can be attempted. The idea is to locally assess (calibrate) this disparity to determine a correction field, which can be used to shift the projection point of a 3D particle to its 'true' position, where it would have been projected without the obstacle. The disparity fields gained from 2D tracking and shown in Figure 10 could already be used for this purpose, as they describe the fine-scale distortions quantitatively for every camera. However, large-scale effects, like lens distortions that are not covered by the 3D camera model are not included in this correction maps. Therefore, a more general approach, using the tracking results of a full 3D STB evaluation is applied. As shown above, despite the small-scale calibration errors introduced by the windows, particle tracking is working successfully, though the 3D positions of the particles will be slightly altered by the calibration errors. The effects of the several cameras will overlap in the volume, possibly reducing this effect to a certain extent. However, in order to accurately calibrate the deflection field, the 3D position should be as accurate as possible.

To further dampen the small scale window-deflections, a similar as introduced for the 2D tracking is applied: The particle trajectories above a certain velocity threshold from a sample run of 800 time-steps (each containing approx. 520,000 particles) are filtered using cubic B-splines ('TrackFit', Geseman et al. 2016) with a low cross-over frequency of 0.05. The found particle positions are back-projected onto the camera images. These 2D positions on the different cameras will show a disparity to the particle peak present at the source image. Averaging these disparities will give a measure for the deflection error at this image location.

In order to calculate the disparity for each individual particle, the peak position of the particle image has to be determined with high accuracy. Typically used peak finding procedures are not suited, as these do not provide the required accuracy and do not work reliably at the high particle image densities present in this case. Instead, a 2D image matching technique is applied, which is closely related to the 3D 'shaking' procedure, which is used at the heart of the IPR (Wieneke 2013, Jahn 2017) and STB methods. In the 2D version (termed '2D-shaking' from here on), not the 3D particle location is altered in order to best match the images of several cameras, but the peak location on a single camera is varied to minimize the local residuum. To this end, a steepest-descent method that uses the gradient of the cost function to analytically derive the optimal step size (Jahn 2017) was used. Using this approach, the projected positions of all particles seen by a certain camera are corrected to best fit the original camera image.

The difference between the original back-projected position and the position determined by 2D-shaking gives the disparity. These disparities are averaged in bins of 10×10 pixels for the whole time-series. On average around 2,000 entries are gathered within each bin. The results for camera A1 to A4 are given in Figure 11. They clearly show a similarity to the 2D-tracking results given in Figure 10 , however now additionally overlapped by large-scale lens-effects.
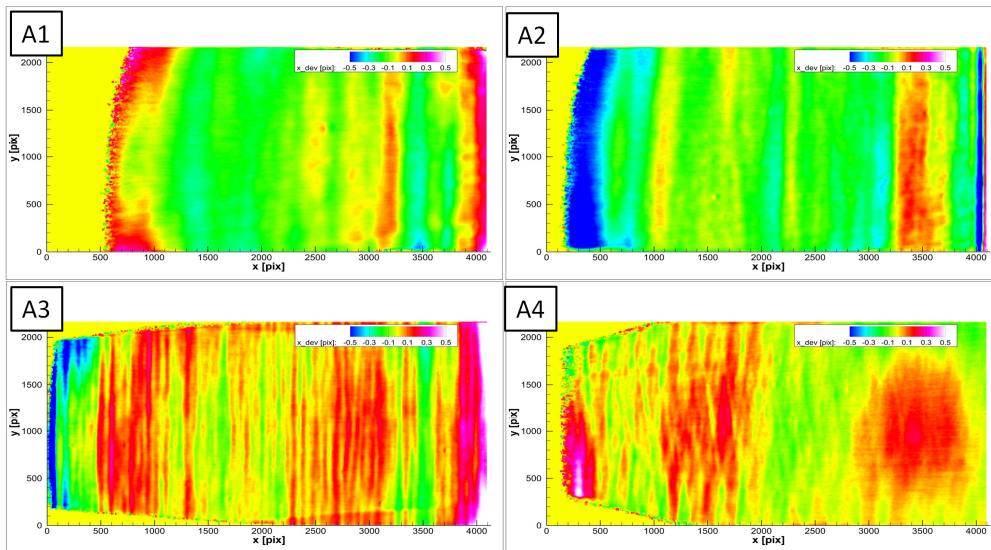
Figure 11: Deflection fields of cameras A1-A4, determined by averaging the disparity between back-projection of fitted 3D tracks and optimal peak position according to the source-images.

The inner parts of the images can show disparities up to 0.3 pixels, at the border values above 0.5 pixels are registered. These border effects are likely caused by lens distortions, which were not captured by the camera model. The two distinct lines of positive and negative disparity at the downstream edge of camera A2 are caused by diffraction from a window frame, which was present in very close proximity to the field of view of this camera. The interplay of the different cameras within the volume is clearly visible in camera A3, where the projected field-of-views of other cameras can be seen as line-patterns overlaying the stripe structure.

Now that we have a well-resolved measure for occurring deflections, we can use these maps to correct the camera calibration. When projecting a location from 3D space to a 2D camera image, the result is simply shifted according to the deflection value at this position given by the calibrated map. When determining a 3D line-of sight from a 2D camera location, the inverse transformation is applied. In order to ensure smooth transitions between the cells (bins), the map is interpolated by a 2D B-Spline field.
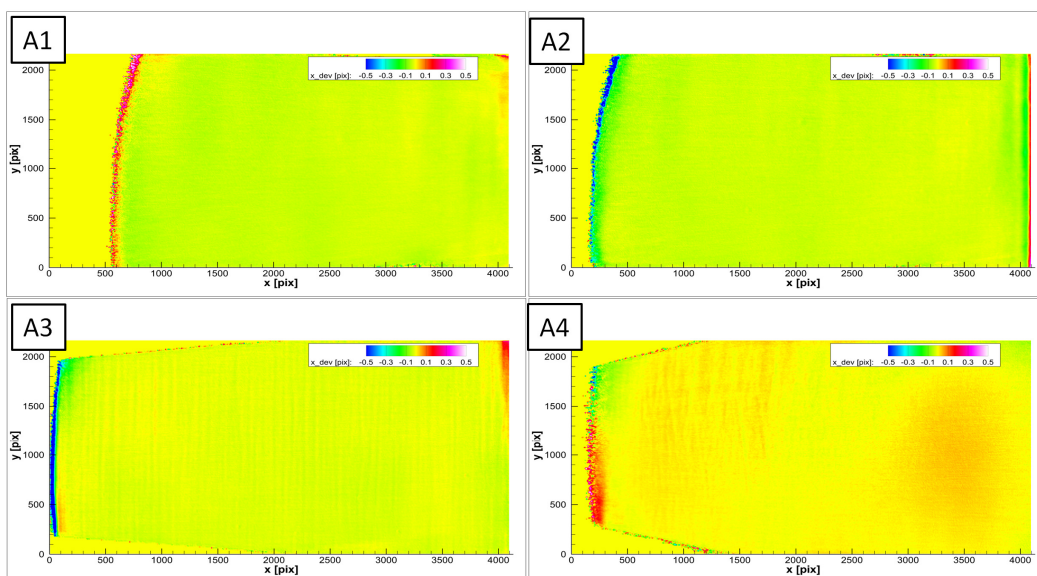

Figure 12: Second iteration of deflection fields of cameras A1-A4

The same time-series of 800 images was re-evaluated using the new, corrected, calibration. The results are shown in Figure 12. It can be seen that the effects were largely corrected. Hints of the underlying patterns still remain though. The maps from this second iteration are added to the original ones, providing the final correction maps. It has been found that the detected deflections are slightly underestimated (likely because the particle position during calibration is still influenced by the deflection, despite the strong temporal filtering). Therefore the correction maps are multiplied by a factor of 1.1, which provides the best results.

These maps are then used to re-evaluate the previous time-series. The averaged accelerations are given in Figure 13 (left). The artificial accelerations caused by the window glass are largely resolved. However, at the transition regions between different cameras the deviations are too severe to be fully corrected by updated calibration. Though the effects are reduced, traces of the particle trajectories exhibiting a jump are still visible as bands of artificial acceleration along the borders of the field-of-view of several cameras.
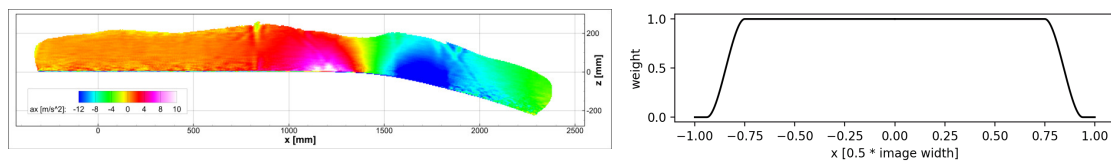

Figure 13: (left) Averaged streamwise acceleration for the same case as given in Figure 8, here with 3D calibration corrected for deflections and camera calibration deviations. (right) Weighting function in relation to normalized x-coordinate of each camera (extending to x = ± 1). The weight is gradually reduced by a smoothstep-function starting at x = ± 0.75 to x = ± 0.94.

In order to further reduce the edge-of-camera effects another measure was introduced. The distinct acceleration bands are caused by the sudden loss of influence of a certain camera on the particle location. Therefore a weighting system was implemented, which regulates the influence of each camera on the shake process of a certain particle, based on the 2D position of the particles projection point on this camera. To this end, a smoothstep-function is used, which reduces the weight from 1.0 in the inner parts of the camera image to down to 0.001 in the last 6 % of the image in x-direction (as the camera systems overlap in this direction). See Figure 13 (right) for a depiction. Evaluating the same time-series as above with this additional weighting applied during the shake-process yields the result shown in Figure 6 (bottom) in the results section, where the influence of the camera transitions has been reduced to a negligible level. The acceleration peak at the onset of the FPG region is now clearly defined, as well as the deceleration region where the FPG transitions into the APG. The FPG region is now nearly void of artefacts.

4 Conclusions

A large-scale time-resolved experimental investigation on a turbulent boundary layer in several regimes of pressure gradient has been successfully performed using Shake-The-Box Lagrangian Particle Tracking of Helium-filled soap bubbles with the goal of investigating so-called turbulent superstructures. Hundreds of thousand bubbles could be tracked over a 2.9 m long measurement volume using a system of 12 high-speed cameras.

When using HFSB seeding it can be non-trivial to achieve high seeding densities, especially at higher flow velocities, as the number of nozzles cannot be scaled as easily compared to DEHS seeding generators. Furthermore, wind-tunnel meshes prove to be an obstacle, potentially destroying a high percentage of bubbles. In the current experiment, the maximum spatial resolution could only be achieved by positioning the HFSB nozzle-arrays close to the measurement section, potentially influencing the flow. For the physically more interesting cases, the nozzles had to be moved into the wind tunnel tower, minimizing their impact on the flow, at the cost of reduced bubble concentration. Still, approx. 200,000 bubbles could be instantaneously tracked for these cases at 14

m/s free stream velocity. In order to limit the particle shift at higher velocities, a time-resolved double illumination scheme was applied and the STB evaluation has been modified accordingly.

Large-scale structures can be identified by eye within the particle field. The development of feature detection and tracking methods for these structures is an ongoing work. Interpolation of the discrete particle field using physical constraints (FlowFit) demonstrates that also finer scales can be resolved within such large measurement volumes, providing a sufficient seeding concentration. The interaction of these vortical structures with superstructures can thus be investigated, e.g. their role in transport processes over structure boundaries.

Several optical and experimental effects have been found to interact with the tracking accuracy. Windows placed between the camera sensor and the measurement region introduce distortion and deflection effects. These effects are especially pronounced in large-scale measurements due to the used wide-angle lenses and the large field-of-view on a wind tunnel window. The installed windows did not show any visible defects, therefore it is expected that such effects are widespread when using readily available glass plates (like float glass). Installing Schlieren-free, polished optical glass would minimize distortions, however the cost typically prohibits this solution for large windows. A further deviation is introduced by the use of wide-angle lenses, which can exhibit large-scale distortions that cannot be fully corrected using standard 3D calibration models, most notably at the outer areas of the frame. Lagrangian Particle Tracking methods have become accurate enough to measure such phenomena. The average acceleration is a very sensitive tool for detecting localized calibration (i.e. deflection) errors.

Both of the mentioned effects have been found to be largely 2D (not changing over the depth of the measurement volume). Therefore, a correction method was developed, that relies on calibrating the shift on the different cameras introduced by the different effects. To this end, the particle position was treated by a large-kernel temporal filter, minimizing the position bias. The reprojected particle position is compared to the position of the particle image found on the original image. These are determined by applying an image matching scheme ('2D shaking'). The disparities are averaged in small bins, thus creating a well-resolved correction map to the calibration of each camera.

The updated calibrations effectively reduce the small-scale effects. A special treatment of the edge region of each camera ensures a smooth transition of a particle from being inside and outside the field-of-view of a certain camera. To this end, a smoothstep function gradually reduces the weight of the camera in the shaking process when the particle approaches the edge of the field-of-view.

Acknowledgements

References

Bross M, Fuchs T, and Kähler CJ (2019) Interaction of coherent flow structures in adverse pressure gradient turbulent boundary layers. J. Fluid Mech. In press

Gesemann S, Huhn F, Schanz D, Schröder A, From noisy particle tracks to velocity, acceleration and pressure fields using B-splines and penalties. 18th Laser Symposium, Lisbon, Portugal, 2016

Hutchins N, Marusic I (2007), Evidence of very long meandering features in the logarithmic region of turbulent boundary layers. J. Fluid Mech. 579:1-28

Jahn T (2017) Volumetric Flow Measurement: An implementation of Shake-The-Box. Master thesis, DLR Göttingen (2017)

Jimenez J (1998), The Largest Scales of Turbulent Wall Flows, CTR Annual Research Briefs: 137-54, University, Stanford

Kim KC, Adrian RJ (1999), Very large-scale motion in the outer layer. Phys. Fluids 11: 417-422

Marusic I, McKeon BJ, Monkewitz PA, Nagib HM, Smits AJ, Sreenivasan KR (2010), Wall-bounded turbulent flows at high Reynolds numbers: recent advances and key issues, Phys. Fluids 22, 065103

Novara M, Schanz D, Geisler R, Gesemann S, Voss C and Schröder A (2019) Multi-exposed recordings for 3D Lagrangian particle tracking with Multi-Pulse Shake-The-Box. Experiments in Fluids 60:3

Paolillo G and Astarita T (2019) A Novel Camera Model for Calibrating Optical Systems Including Cylindrical Windows. AIAA 2019-0273

Schanz D, Gesemann S, Schröder A (2016) Shake-The-Box: Lagrangian particle tracking at high particle image densities. Exp Fluids, 57(5)

Schanz D, Gesemann S, Schröder A, Wieneke B, Novara M (2013) Non-uniform optical transfer functions in particle imaging: calibration and application to tomographic reconstruction. Meas Sci Technol 24:024009

Schröder A, Schanz D, Geisler R, Gesemann S, Willert C (2015) Near-wall turbulence characterization using 4D-PTV Shake-The-Box. 11th International Symposium on Particle Image Velocimetry – PIV15

Stasicki B, Schroder A, Boden F, Ludwikowski K (2017) High-power LED light sources for optical measurement systems operated in continuous and overdriven pulsed modes, Optical Measurement Systems for Industrial Inspection X 10329, 103292J

Wieneke B (2007) Volume self-calibration for 3D particle image velocimetry. Exp Fluids 45:549–556

Wieneke B (2013) Iterative reconstruction of volumetric particle distribution. Meas Sci Technol 24:024008